

Physics through the microscope

Stephen J. Pennycook, Ryo Ishikawa, Haijun Wu(武海军), Xiaoxu Zhao(赵晓续), Changjian Li(黎长建), Duane Loh, Jiadong Dan, and Wu Zhou(周武)

Citation: Chin. Phys. B, 2024, 33 (**11**): 116801. DOI: 10.1088/1674-1056/ad7aff
Journal homepage: http://cpb.iphy.ac.cn; http://iopscience.iop.org/cpb

What follows is a list of articles you may be interested in

Real-time four-dimensional scanning transmission electron microscopy through sparse sampling

A W Robinson, J Wells, A Moshtaghpour, D Nicholls, C Huang, A Velazco-Torrejon, G Nicotra, A I Kirkland, and N D Browning

Chin. Phys. B, 2024, 33 (**11**): 116804. DOI: 10.1088/1674-1056/ad8a4a

Multidimensional images and aberrations in STEM

Eric R. Hoglund and Andrew R. Lupini

Chin. Phys. B, 2024, 33 (**9**): 096807. DOI: 10.1088/1674-1056/ad73b2

Multiphase cooperation for multilevel strain accommodation in a single-crystalline $BiFeO_3$ thin film

Wooseon Choi, Bumsu Park, Jaejin Hwang, Gyeongtak Han, Sang-Hyeok Yang, Hyeon Jun Lee, Sung Su Lee, Ji Young Jo, Albina Y. Borisevich, Hu Young Jeong, Sang Ho Oh, Jaekwang Lee, and Young-Min Kim

Chin. Phys. B, 2024, 33 (**9**): 096805. DOI: 10.1088/1674-1056/ad62e0

Symmetry quantification and segmentation in STEM imaging through Zernike moments

Jiadong Dan, Cheng Zhang, Xiaoxu Zhao(赵晓续), and N. Duane Loh

Chin. Phys. B, 2024, 33 (**8**): 086803. DOI: 10.1088/1674-1056/ad51f4

Anomalous strain effect in heteroepitaxial $SrRuO_3$ films on (111) $SrTiO_3$ substrates

Zhenzhen Wang(王珍珍), Weiheng Qi(戚炜恒), Jiachang Bi(毕佳畅), Xinyan Li(李欣岩), Yu Chen(陈雨), Fang Yang(杨芳), Yanwei Cao(曹彦伟), Lin Gu(谷林), Qinghua Zhang(张庆华), Huanhua Wang(王焕华), Jiandi Zhang(张坚地), Jiandong Guo(郭建东), and Xiaoran Liu(刘笑然)

Chin. Phys. B, 2022, 31 (**12**): 126801. DOI: 10.1088/1674-1056/ac8725

TOPICAL REVIEW — Stephen J. Pennycook: A research life in atomic-resolution STEM and EELS

Physics through the microscope

Stephen J. Pennycook[1,2,†], Ryo Ishikawa[3], Haijun Wu(武海军)[4], Xiaoxu Zhao(赵晓续)[5], Changjian Li(黎长建)[6], Duane Loh[7,8], Jiadong Dan[7,8], and Wu Zhou(周武)[1]

[1] *School of Physical Sciences and CAS Key Laboratory of Vacuum Physics, University of Chinese Academy of Sciences, Beijing* 100049, *China*
[2] *Department of Materials Science and Engineering, University of Tennessee, Knoxville, TN*, 37996, *USA*
[3] *Institute of Engineering Innovation, University of Tokyo, Tokyo* 113-8656, *Japan*
[4] *State Key Laboratory for Mechanical Behavior of Materials, Xi'an Jiaotong University, Xi'an* 710049, *China*
[5] *School of Materials Science and Engineering, Peking University, Beijing* 100871, *China*
[6] *Department of Materials Science and Engineering, Southern University of Science and Technology, Shenzhen* 518055, *China*
[7] *Department of Physics, National University of Singapore, Singapore* 117551, *Singapore*
[8] *Department of Biological Sciences, National University of Singapore, Singapore* 117558, *Singapore*

(Received 27 July 2024; revised manuscript received 9 September 2024; accepted manuscript online 14 September 2024)

The electron microscope provides numerous insights into physics, from demonstrations of fundamental quantum mechanical principles to the physics of imaging and materials. It reveals the atomic and electronic structure of key regions such as defects and interfaces. We can learn the underlying physics governing properties, and gain insight into how to synthesize new materials with improved properties. Some recent advances and possible future directions are discussed.

Keywords: scanning transmission electron microscopy, materials science, point defects, artificial intelligence

PACS: 68.37.Ma, 87.64.Ee, 81.07.–b, 47.54.Jk **DOI:** 10.1088/1674-1056/ad7aff

1. Introduction: The physics of imaging

It is less than a century since the invention of the electron microscope and its impact on physics has been profound. Many classic demonstrations of the principles of quantum mechanics have been performed on the transmission electron microscope, including the Aharonov–Bohm effect[1] and wave–particle duality.[2,3] A simple thought experiment demonstrates the central quantum-mechanical nature of the electron microscope. In Fig. 1 we see the basic elements of an electron microscope. At a typical probe current of 160 pA, electrons hit the specimen every 10^{-9} s. 200 kV electrons travel at about 200000 km/s, and are therefore on average 2 cm apart in the column. For a sample to be electron transparent, it must be of the order of 100 nm thick or less, hence we see immediately that there is very little chance of two electrons being in the specimen at the same time. Electron microscopy is based on the scattering of individual electrons, one by one.

That scattering creates a diffraction pattern, which the microscope can focus onto a screen or detector. The diffraction pattern is also built up from individual electrons striking the detector at some location. In the imaging mode of a transmission electron microscope (TEM), the diffraction pattern is refocused back into a real space interference pattern. Again, each electron strikes the detector at some location, one at a time, and it is only with large numbers of electrons that the pattern appears as a set of interference fringes. But the probability of any one electron striking the detector is still governed by the interference between all the different potential scattering pathways. This wave–particle duality is the essential characteristic of quantum mechanics, and was clearly demonstrated with Young's fringes in the electron microscope.[2,3] Each electron strikes the screen according to the probability distribution, but we cannot predict exactly where it will strike until the electron does actually strike the screen or detector. This has another important consequence, that the momentum transfer to the specimen cannot be determined until the electron does strike the screen, when the wave function is said to collapse. With a typical distance from sample to detector of 1 m or so (see Fig. 1), this collapse occurs ~ 5 ns after the electron traversed the specimen. This is the essence of quantum mechanical non-locality, another strange aspect of quantum mechanics, that the outcome of the scattering is not determined until long after the electron passed through the sample.

Another consequence of electrons propagating as probability amplitudes is the distinction between coherent and incoherent imagings. As first pointed out by Lord Rayleigh for light microscopy,[4] incoherent imaging means that only the intensity illuminating a point on the object determines the intensity in the image. Phases do not need to be considered. The image is a rendition of the object just blurred by the resolution function of the microscope. Therefore, a direct relationship exists between the object and image and given sufficient resolution a direct interpretation of the image can be made.

[†]Corresponding author. E-mail: stevepennycook@gmail.com

© 2024 Chinese Physical Society and IOP Publishing Ltd

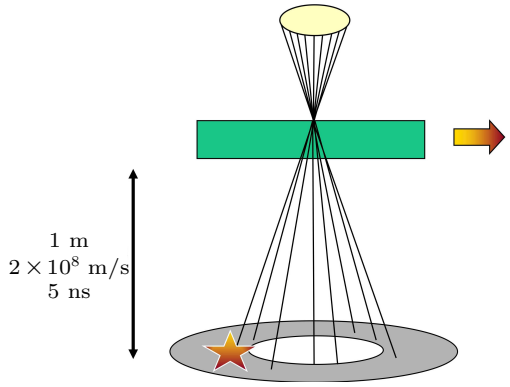


Fig. 1. Schematic indication of a probe being scattered by a specimen, followed by propagation to the detector. All scattering paths are possible with their respective probabilities, but only when the electron reaches the detector does the wave function collapse, the direction of momentum transfer becomes determined, and the sample recoils, about 5 ns after traversing the sample.

The same is true for imaging with electrons, except, historically, coherent imaging was developed first. If the diffracted beams emerging from the specimen are refocused onto a screen, an interference pattern is formed where the contrast depends on their relative phases, which also depends on factors such as specimen thickness and lens focus. Changes in either may result in contrast reversals so image interpretation is not always trivial, especially if resolution is limited. It took a long time to appreciate how incoherent imaging could be achieved with electrons, using the high angle electron scattering in a scanning transmission electron microscope (STEM).[5,6] And longer still before it could be achieved efficiently with aberration corrected microscopes.[7] This story has been reviewed previously and we will only briefly mention a few key highlights below.

Quantum mechanics also connects the two major forms of microscope, the fixed beam TEM and the STEM, through time reversal symmetry.[8,9] This is a key principle of physics, a fundamental property of elastic scattering amplitudes.[10,11] It means that if a wave is reversed to travel in the opposite direction the scattering amplitude of any object will be the same. Elastic scattering is responsible for most contrast in electron microscope images, and how this principle links image formation in TEM and STEM can be appreciated from Fig. 2. A bright field STEM image with a small axial detector shows the same contrast as a TEM image (whether a diffraction contrast image or a lattice image) because the ray paths and interference are identical, just reversed. Both are therefore coherent images, which is easily appreciated from the TEM case, where the object is illuminated by a plane wave, or close approximation. By reciprocity, the STEM bright field image is also a coherent image. Incoherent imaging is achieved by the annular dark field (ADF) detector in STEM, which detects a large angular range of diffracted beams and so detects the total scattered intensity that falls on it. Interference does not change the total scattered intensity, just redistributes it, so the annular detector gives an image with incoherent characteristics, just like seen in a normal camera, with no reversals of contrast. If we reverse the STEM ray paths to the TEM case we can see that the large detector acts essentially as Lord Rayleigh described for the condenser lens in light microscope illumination, providing multiple phases illuminating each point in the image. It is just because large condenser apertures cannot be readily achieved in TEM with simultaneous large fields of view that the TEM does not generally employ this mode of imaging, and is limited to coherent imaging. Since high angle scattering is largely Rutherford scattering from the atomic nuclei it is strongly dependent on atomic number Z, so the high angle annular dark field (HAADF) image is dominated by atomic number or Z-contrast.

Another difference concerns the highest available resolution, which is determined by the wavelength λ and the largest scattering angle contributing to the image. In the TEM case of Fig. 2(a), the largest angle is the radius of the objective angle θ, but in the STEM case interference can occur across the entire aperture diameter 2θ, double the resolution. This basic imaging physics is also true for light microscopy. Another difference concerns the size of the atom, as contributing to the image. The object for TEM imaging is the atomic potential, but for HAADF imaging it is the screened nuclear potential, significantly narrower.[12]

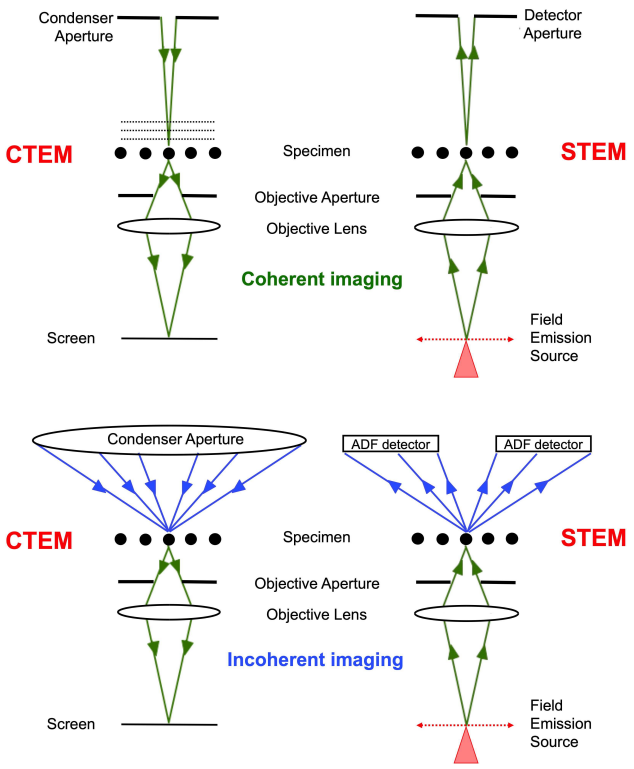


Fig. 2. Ray diagrams for coherent (upper) and incoherent (lower) imaging in the TEM (left) and STEM (right) showing the reciprocity between the two microscopes. Reciprocity holds no matter how many additional optical elements are present, round lenses or aberration correctors.

So we see that the STEM provides two complementary views of the specimen just by using two simultaneous detectors, one an incoherent, *Z*-contrast image using the ADF detector, and a phase contrast image with a small axial detector. Many other possibilities exist, and an especially useful one is annular bright field (ABF) imaging. An annular detector is used, with the collection angle ranging from about half the radius of the objective aperture to near the full angle. It is therefore a bright field image, but because of the significant angular integration over the detector it gives quite incoherent characteristics, providing easily interpretable images over a significant range of thickness and defocus.[13,14] It is also highly complementary to the HAADF image, being much less *Z*-dependent and allowing visualization of heavy and light elements simultaneously. With the use of 4D STEM, where the detectors are replaced by a camera detecting all points in the diffraction pattern simultaneously, many more possibilities exist, as we discuss later. Furthermore, inelastic analytical signals are also available with the same probe, at atomic resolution, not only elemental composition via x-ray detection or electron energy loss spectroscopy (EELS) but also valence from EELS fine structure, and even vibrational properties from low loss EELS.

2. Key milestones in the history of STEM

The invention of the TEM by Ernst Ruska and Max Knoll in 1931 is well known,[15] resulting in the Nobel Prize in physics in 1986. However the invention of the STEM by Baron Manfred von Ardenne in 1938 is less well known,[16] because it was not possible to form a probe with enough current to provide a good quality image. Von Ardenne soon abandoned the STEM in favor of the TEM, and it was not until almost 30 years later that a successful STEM was developed by Albert Crewe.[17] The key to success was his development of the cold field emission gun, a high brightness electron source that enabled a small enough probe to be formed to image individual atoms.[18] For a detailed history of the development of STEM see Ref. [19].

More years would pass before a commercial STEM could achieve atomic resolution. John Cowley showed an ADF image of $Ti_2Nb_{10}O_{29}$ showing improved atomic resolution detail in the dark field image, using a VG Microscopes HB5 STEM with a modified pole piece.[20] VG Microscopes later produced their own high resolution pole piece, and an example of atomic resolution imaging is shown in Fig. 3, comparing HAADF images of Si and InP in ⟨110⟩ zone axis orientation.[21] The characteristics of incoherent imaging were already clearly seen. In this orientation, the crystal appears as two closely spaced atomic columns, as shown by circles, and although they are not resolved in Si, it is clear that each column is contributing to the image intensity because the dumbbells appear as oval features. In an incoherent image, the image features are reproduced faithfully even below the resolution limit. In the InP case, we see the dominance of the heavy In columns, the crystal appearing as almost circular features with the lighter P columns barely contributing. Insets show simulations, performed by a simple convolution of a probe intensity profile with a high angle scattering cross section, another characteristic of incoherent imaging.

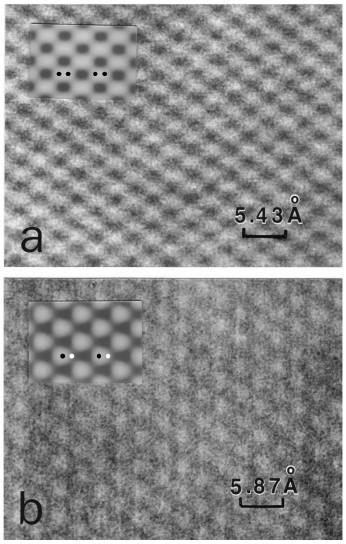


Fig. 3. HAADF images of (a) Si and (b) InP in ⟨110⟩ orientation, with Si and In columns indicated by black dots and P columns as white dots. Adapted from Ref. [21].

A few years later, when a 300 kV STEM became available, the probe size reduced enough to directly resolve such dumbbells.[22] Many materials revealed their secrets at this time, including quasicrystals,[23] semiconductor interfaces,[24] catalysts[25] and grain boundaries.[26] Atomic resolution spectroscopy was also achieved, using the *Z*-contrast image to accurately locate the probe over atomic columns while EELS was performed.[27]

A new era for electron microscopy was ushered in by the successful correction of lens aberrations, which had been a dominant limitation to resolution since the invention of the microscope. Suddenly, sub-Ångstrom resolution could be obtained,[28,29] and spectroscopic sensitivity was enhanced to single atom identification.[30] Today we are in the second generation of aberration correctors, able to correct aberrations up to the 5th order, further increasing not just resolution but also image contrast, giving the ability to separate closely spaced columns with high contrast and to see light atoms next to heavy ones. *Z*-contrast images were even able to image atoms as light as graphene,[31] and not only to identify individual impurity atoms by spectroscopy, but from the fine structure, even determine the nature of their bonding. Figure 4 shows identification of Si in two different configurations in graphene, the threefold case being sp^3 bonded, as in bulk SiC, the fourfold case being sp^2d bonded, to utilize the geometric shape of d-orbitals.[32]

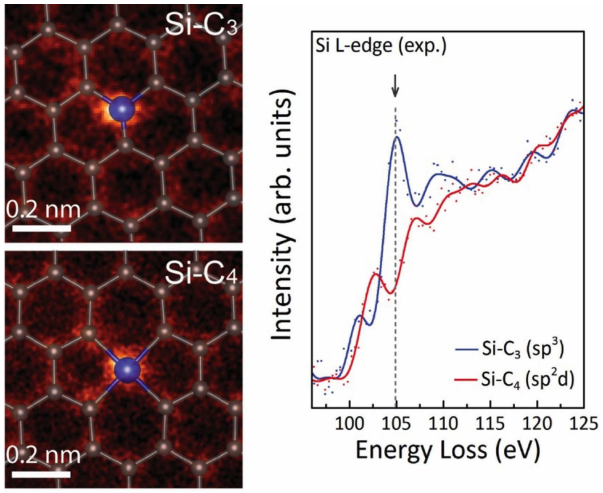


Fig. 4. Images of 3- and 4-fold bonded C atoms in monolayer graphene with corresponding EELS spectra. From the fine structure the nature of the bonding can be inferred. Adapted from Ref. [32].

We also learned that with small probes, good image quality could be achieved with smaller beam currents. Beam damage could be reduced so as not to immediately amorphize susceptible samples, or sometimes eliminated completely by reducing the accelerating voltage to below the damage threshold. Damage sometimes actually became visible in the form of atomic motions between successive frames, allowing fundamental physical processes such as diffusion to be observed for the first time. Figure 5 shows Ce diffusing through AlN, where processes that had previously been proposed theoretically could be directly visualized, including the interstitial kick-out mechanism and correlated vacancy–impurity exchange.[33]

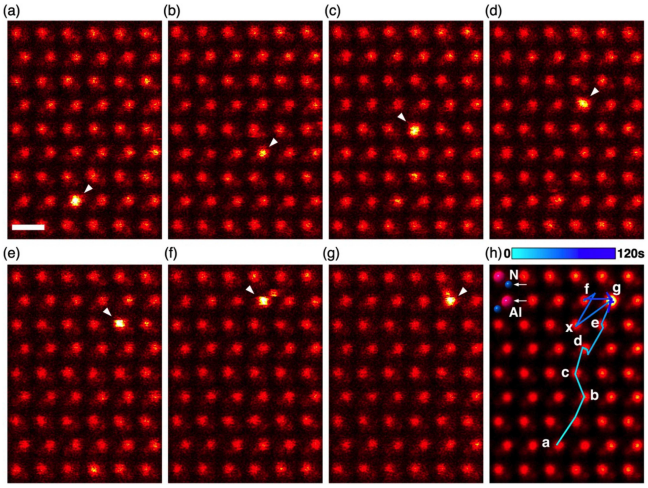


Fig. 5. Selected frames from a sequence of 30 *Z*-contrast images of a *w*-AlN single crystal doped with Ce viewed along the $11\bar{2}0$ axis. (a)–(g) Frames 1, 4, 5, 6, 10, 16, 20, respectively, show the locations of a single Ce dopant as marked by the arrowhead in each panel. (h) Frame-averaged *Z*-contrast image. The observed Ce trace is overlaid and the Ce positions in each panel (a)–(g) are indicated. The scale bar in (a) is 3 Å. Reproduced from Ref. [33].

3. New insights into materials

Microscopists have long claimed that if we could see the details of a material's microstructure then we would understand the origin of its properties and see the path forward to improving those properties. Aberration-corrected STEM has now given us that ability, so has this actually led to new materials' properties? We mention just a few examples that have changed our thinking, influenced the future direction of research in their fields, and some that have indeed led to record materials performance.

The first concerns solar cells, specifically CdTe, and the role of grain boundaries; in particular, the role of the Cl heat treatment in bringing efficiency to practical levels. Historically considered deleterious to solar cell efficiency, materials efforts focused largely on avoiding grain boundaries as much as possible. However, STEM imaging, together with electron-beam-induced-current (EBIC) imaging of bulk cross section samples in a scanning electron microscope, instead indicated that after the Cl heat treatment boundaries actually improve current collection. The reason was uncovered by atomic resolution studies in STEM, as shown in Fig. 6. The boundary is seen to be built from structural units comprising one Ti column surrounded by three Cd columns. The EELS line trace shows Te depletion and Cl enrichment at the grain boundary, indicating Cl substitution for Te. The result was the same for boundaries of any geometry, indicating a general phenomenon. Density functional calculations showed that the Cl doping doped the boundary n-type, creating mini p–n junctions within the material therefore enhancing current collection.[34]

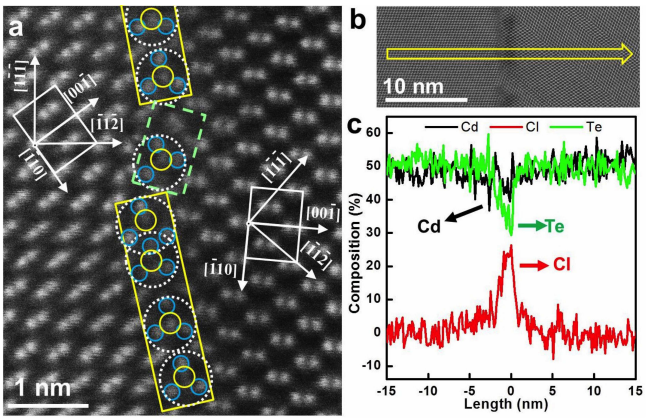


Fig. 6. Atomic structure and elemental distribution at a grain boundary in a $CdCl_2$-treated CdTe solar cell. (a) STEM *Z*-contrast image showing a Σ9 grain boundary with symmetric and asymmetric segments indicated by yellow and green dashed boxes, both comprising the same structural units, Cd_3Te dislocation cores (white dashed circles). The small blue and large yellow solid circles indicate single Cd and Te columns, respectively. (b) An EELS line scan was taken along the yellow arrow, and (c) the resulting composition profiles show strong Cl enrichment and Te reduction confined to a 1–2 nm range at the GB. Adapted from Ref. [34].

Piezoelectrics are another area of functional materials where properties arise from complex microstructures that are difficult to unravel. Figure 7 shows how increasing spatial resolution from TEM images through convergent beam electron diffraction (CBCED) patterns to phase identification at the unit cell level reveals a complex, hierarchical nanodomain

structure.[35] Such structures were found common to numerous different materials, and show that the coexistence of multiple phases, with nearly degenerate energies, and hence minimal domain boundary energy that allows easy boundary migration and polarization rotation. Hence the microstructural origins of good piezoelectric response were able to be uncovered to guide future materials development.

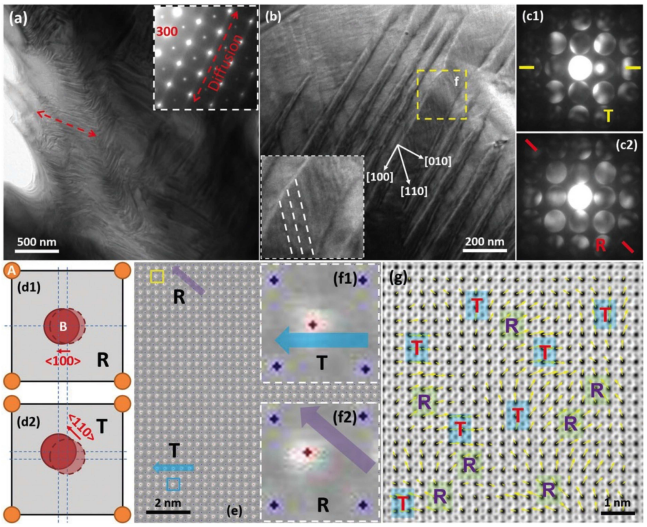


Fig. 7. Nanodomains and local structure of (K,Na)NbO_3-based piezoelectric material. (a) TEM image showing slim nanodomains without submicron domains. (b) TEM image showing the hierarchical nanodomain structure, with an enlarged image inset. (c1) and (c2) CBED patterns from adjacent nanodomains showing mirror planes along ⟨100⟩ and ⟨110⟩ for tetragonal T phase and rhombohedral R phase, respectively. (d1) and (d2) Schematics showing T and R symmetries with B atom displacement along pseudocubic axes and diagonals with respect to A atoms, respectively. (e) Atomically resolved STEM HAADF image with atom positions and R and T regions marked. (f1) and (f2) Enlarged images of the regions marked in (e), showing T and R symmetries. (g) Atomically resolved STEM annular bright field image with arrows representing displacements of the center Nb columns with respect to O columns. Reproduced from Ref. [35].

Epitaxial thin film piezoelectric materials have historically had much poorer properties than their bulk counterparts, but this has dramatically changed in the last few years. $NaNiO_3$ thin films having record piezoelectric response have been engineered by deliberately growing Na-deficient films, which introduces translational domain boundaries to accommodate the non-stoichiometry. These boundaries are the source of the outstanding response, double that of the best Pb-based thin film.[36] Soon after this discovery, it was found that just by increasing the density of the nanodomains, the response doubled yet again.[37] Furthermore, along with the large response came a robust temperature dependence. This success story suggests that similar strategies could be employed for other functional thin film systems.

Another area that has seen a surge of activity in recent years is 2D materials. Not only do these materials demonstrate a wealth of fascinating new physics but they also have numerous practical applications. Microscopy is invaluable for phase and defect identification,[38] and can again lead to insights into new directions for synthesis. One example is the intercalation of species into the Van der Waals gaps, leading to dramatic changes in properties. When grown in metal-rich conditions, the excess metal atoms tend to fill the octahedral vacancies in the Van der Waals gaps, and with the right ratio they form ordered arrays that exhibit new properties such as ferromagnetism. Figure 8 shows an example of an ordered intercalated array of 33% Ta in Ta_7S_{12}, where the intercalated Ta occupies a $\sqrt{3} \times \sqrt{3}$ superstructure and gains a magnetic moment.[39] Based on these observations we can speculate upon whole new classes of other intercalated 2D materials.

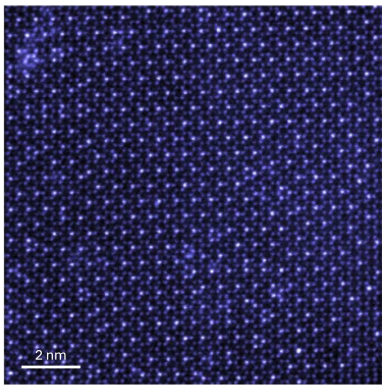


Fig. 8. Use of non-stoichiometric growth to create a self-intercalated superlattice of Ta in Ta_7S_{12}. Reproduced from Ref. [39].

A remarkable success story in explaining macroscopic properties through microscopy concerns monolayer amorphous carbon. These structures are produced by chemical vapor deposition, and have very different properties depending on growth temperature. In particular, a remarkable nine orders of magnitude change in sheet resistance occurs on raising the growth temperature by just 25 °C.[40] Figure 9 shows images of two samples grown at 300 °C and 400 °C. Both samples contain distorted crystallites embedded within regions of a continuous random network of 5-, 6- and 7/8-fold carbon rings. However, the sample grown at low temperature is semiconducting, with a temperature dependence indicating hopping conduction, whereas the sample grown at the higher temperature is highly insulating. It is clear from the atomic resolution images that the low temperature sample has larger crystallites, but they are not connected like in graphene, hence the sample is not metallic. Furthermore, the diffraction patterns show no spots, implying both samples to be disordered, but the width of the amorphous rings is sharper in the low temperature sample, showing it to have a lower degree of disorder. Surprisingly, the huge resistance change can be explained by a variable-range hopping model of conducting crystallites embedded in an insulating matrix. Using the images to define the density of disconnected, non-conducting sites, the theoretical resistance–temperature curves could be well matched to those measured experimentally, and a similar huge conductance transition was found in the simulations.

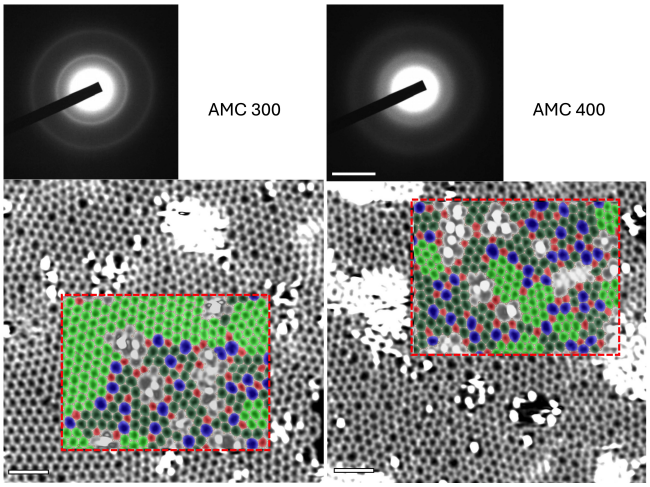


Fig. 9. Images and selected area diffraction patterns of amorphous monolayer carbon grown at 300 °C (left) and 400 °C (right), with 6-fold carbon rings in green, light green in connected regions, dark green in disconnected (insulating) regions, defined as a 6-fold ring with less than 6 neighboring rings. 5-fold rings are shown in red and 7/8-fold rings in blue. Adapted from Ref. [40].

The microscope itself can also be used to create metastable 2D materials. At low beam energies, the two species in a binary 2D material may show very different tendencies for beam damage. This is the case for $MoSe_2$, where the lighter Se atoms are preferentially sputtered by the beam. The Se vacancies tend to attract each other, as seen directly in STEM movies of successive frames, and create regions of monolayer Mo,[41] which we might call a molene by analogy with graphene, as shown in Fig. 10. These regions are sufficiently stable to allow EELS to be performed, showing that no O or C is present to stabilize the Mo film. Density functional calculations further showed that the molene is indeed a metastable form of Mo, albeit in hexagonal arrangement unlike Mo metal which is body centered cubic. The lattice parameter of free-standing molene is 2.7 Å experimentally, compared to a Mo–Mo spacing of 3.3 Å in the $MoSe_2$ film, implying significant tensile forces on the metal monolayers. Indeed, as they grow larger they tend to fracture.

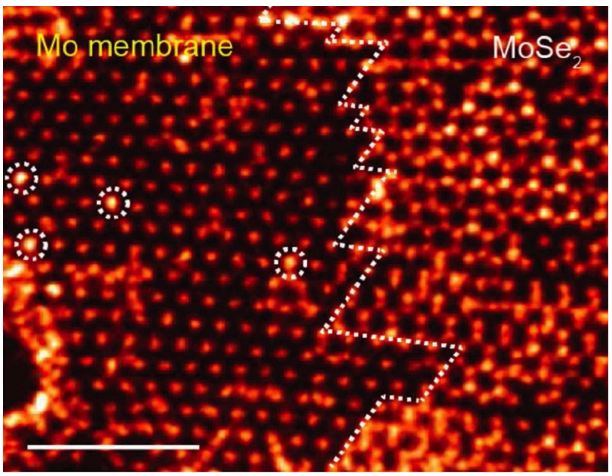


Fig. 10. Formation of a monolayer Mo membrane by sputtering in a STEM. Adapted from Ref. [41].

4. Recent developments: Towards three dimensions

The most significant instrumental development in recent years has been the huge advance in detector technology, with pixelated detectors reaching single electron sensitivity, allowing detector configurations to be chosen after scanning, and simultaneous Z-contrast images with the HAADF detector. Pixelated detectors are not limited to circular geometry, so as well as bright field, low-angle ADF and annular bright field (ABF), many other modes become feasible, including differential phase contrast and its integrated forms that enable electric fields and total charge to be determined at atomic resolution.[42,43]

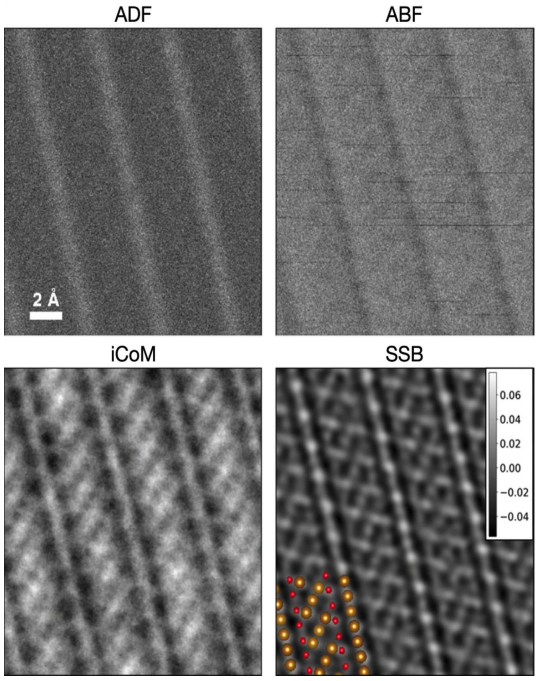


Fig. 11. Simultaneous ADF, ABF, integrated center of mass (iCoM) and SSB ptychography images of Fe_3O_4 acquired with a 2 microsecond dwell time scan. The 4D STEM data were collected on a Timepix3 event driven camera, allowing a rapid scan speed. At the 10000 $e^-/Å^2$ dose used here the dose efficiency of the SSB ptychography is clearly higher than the other imaging methods, showing all the atomic columns, including the light O atoms which are particularly challenging for the ADF signal when neighboring heavier columns such as the Fe columns here, even at far higher doses. Reproduced from Ref. [47].

Collecting low angle scattering is much more dose efficient than limiting the signal collection to only that small fraction at high angles. The most dose-efficient of all is ptychography, because it only utilizes the part of the diffraction pattern that gives a specific spatial frequency, the so-called overlap regions between diffraction discs.[44–46] The remainder is not used, hence the signal to noise ratio is improved. Moreover, in the single-sideband (SSB) method, the resolution cutoff is the diameter of the objective aperture, and the contrast transfer function is single signed, without oscillations. These characteristics are similar to those of the incoherent HAADF image, but with higher signal level. In the example shown in Fig. 11,

the electron dose is so low that the resolution of the HAADF image is limited by noise, not the size of the scanning probe, but it is useful in providing an independent signal confirming the identification of the heavy atoms.[47] The ptychography provides a much more dose efficient image that clearly reveals the light oxygen atoms in the structure. With event-driven detectors, it is no longer necessary to read out empty pixels, and fast scanning is possible.[48] However, unlike the HAADF image, ptychography is still a phase contrast technique and contrast reversals do occur with increasing thickness due to phase-wrapping.

With iterative reconstruction techniques even more can be achieved, albeit at the cost of significantly increased computation time. When overlapping diffraction discs reach the detector, the resolution limit becomes the maximum angle of the detector, not the probe. With enough signal, resolution of the reconstruction can reach several times the diffraction limit into the deep sub-Ångstrom range.[49] The issue with thickness can also be overcome by so-called multislice ptychography,[50] which solves for the object at multiple depths and markedly increases the quality of the reconstruction. Local sample tilt can also be incorporated into the modeling, greatly reducing the sensitivity to small crystal tilts and deformed columns near defects.[51]

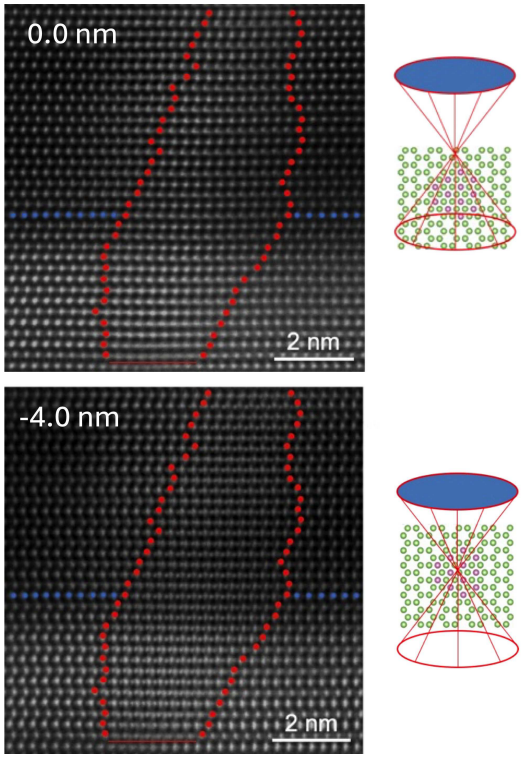


Fig. 12. HAADF images from a cross section of a GaN/InGaN quantum well light emitting device, at defocus of zero and −4 nm. The In rich quantum well is seen brighter. At zero defocus, the beam is focused above a buried stacking fault (see schematic) which is not visible in the image. The atom columns marked by blue dots continue right across the region outlined in red, which contains the fault. When the focus is changed to −4 nm, the columns between the red lines are doubled, marking the overlap of the faulted and perfect regions of crystal. Adapted from Ref. [53].

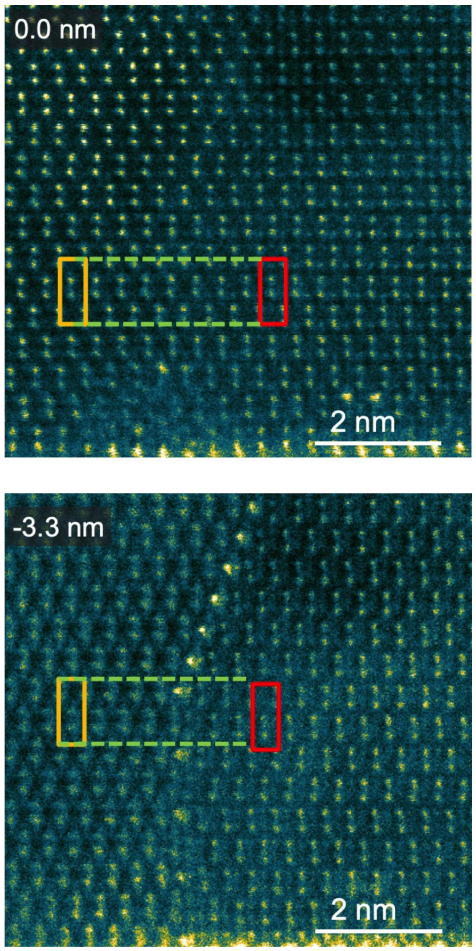


Fig. 13. Cross section views of a TiO_2 anatase thin film grown on a $LaAlO_3$ substrate. The red and yellow boxes mark the unit cell of the anatase. The fault is again buried below the surface, and at zero defocus it is not visible; the red and yellow boxes are perfectly aligned with each other and the crystal appears perfect. At −3.3 nm focus, however, the fault is in focus, and the red and yellow boxes are now displaced either side of the fault line, which is now clearly visible and seen to be decorated with La dopants. Courtesy Changjian Li.

An alternative means to overcome thickness dependent dynamical diffraction effects is to realize that dynamical scattering occurs only close to the zone axis. With 5th order aberration correctors, corrected probes can be formed with 50 mrad convergence at 200 kV. In this case only the central zone undergoes dynamical diffraction and the rest is so far from the zone axis that it propagates as in free space, coming to a focus at a specific depth inside the crystal. The depth of focus is $\lambda/2\theta^2$, which for the conditions mentioned above is close to 0.5 nm. In practice, the depth resolution is also sensitive to the chromatic energy spread of the beam, but we still expect nm scale depth resolution for a cold field emission gun without monochromator.[52] This has indeed proved to be the case, even in quite thick crystals. as shown in Figs. 12–14. Compared to tilt series tomography, optical sectioning has greater lateral resolution but poorer depth resolution. Its major advantage is that no mechanical tilt is required, depth sectioning being achieved simply by changing the focus of the objective lens.

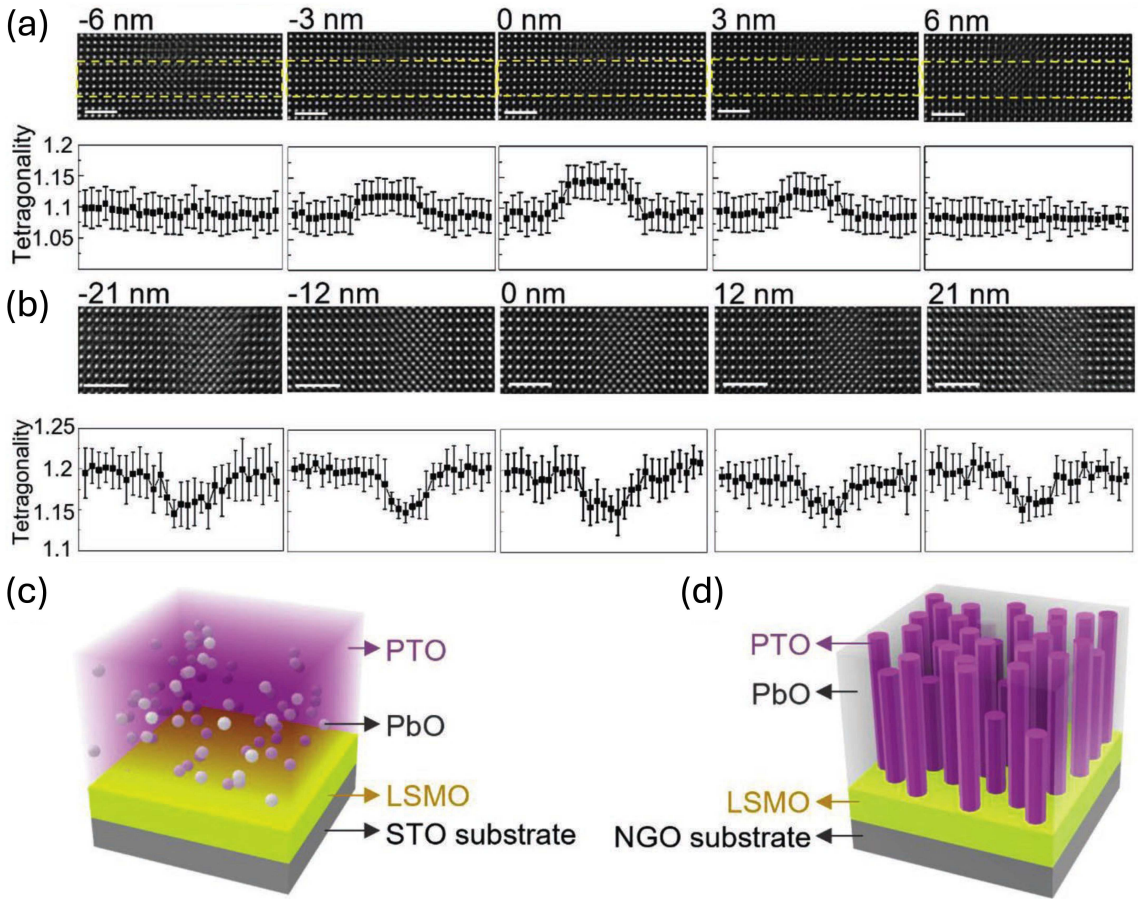


Fig. 14. Depth sectioning in $PbTiO_3$(PTO)/PbO composite systems prepared in nano-spherical (a), (c) and nanocolumnar (b), (d) configurations. The depth resolved unit-cell by unit-cell tetragonality profiles (a) and (b) highlight the different morphologies very clearly, with tetragonality extending for a depth of over 40 nm in the nanocolumnar sample. This creates a giant c/a ratio and a polarization three times the bulk value. Adapted from Ref. [54].

5. Future outlook

What developments might we expect in the coming years? It is difficult to predict breakthroughs, but it is interesting to speculate on some issues that might change the way microscopy is done, and perhaps therefore change the way materials science and maybe even biological science is performed. First, let's ask what might happen to depth resolution if we were to double the size of the objective lens to 100 mrad semi-angle. Right now this can only be done in simulations, but they suggest that atomic resolution in depth becomes possible, as shown in Fig. 15. If this was to be achieved, it might be advantageous to tilt off the zone axis, since no channeling is required, indeed none is desired, and this would increase the depth between single atoms at any given probe position. In fact, it would not even be necessary to have a crystalline sample, and a whole range of amorphous and nanophase materials would be amenable to investigation, atom by atom, in three dimensions.

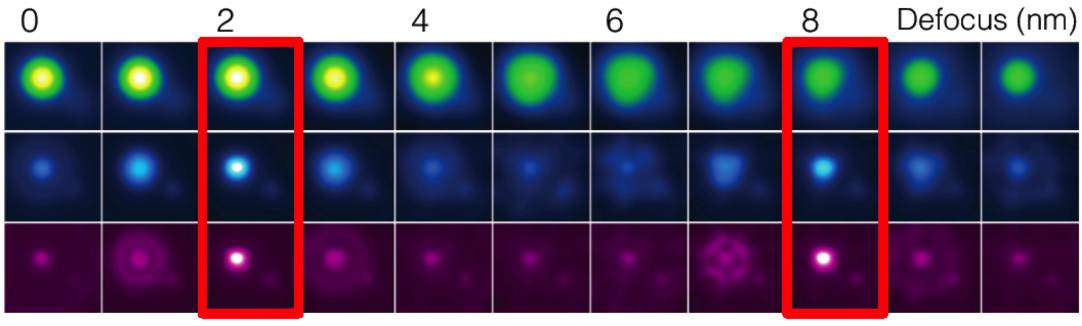


Fig. 15. Simulated focal series of images of Ce atoms substituted in AlN for 0–10 nm defocus with probe-forming angles of 30 mrad (upper), 60 mrad (center) and 100 mrad (lower) at 300 kV accelerating voltage, assuming aberration free conditions. Ce atom locations are indicated by red rectangles. They are well-resolved in depth even at 60 mrad convergence semiangle. Reproduced from Ref. [55].

We have seen how piezoelectrics has benefited from clear atomic resolution images, leading to record properties. Similar advances have occurred in thermoelectrics, another area with important practical applications, but these materials also have very complex microstructures. This stems from the need to minimize phonon transport, needing scattering centers at multiple length scales, from atomic-scale point defects to precipitates and grain boundaries, while simultaneously maximizing electron transport. Some major advances have been made, from synergistic optimization[56] to using entropy,[57] but could we actually measure properties locally? With monochromated electron guns it has been possible to resolve phonon peaks in EELS, not only the energy loss peaks but also the energy gain peaks, where a preexisting phonon is absorbed by the beam and so increases its energy. The ratio of these two processes depends on temperature, and with a nanoscale beam, nanoscale temperature measurement can be achieved.[58] Perhaps local temperature mapping could reveal the thermal influence of extended defects, such as the Van der Waals gaps in GeTe,[59] although higher temperature sensitivity is probably necessary.

We have already seen how the electron beam can be used to fabricate a metastable monolayer material, but can the beam be used for atom-by-atom fabrication? Remarkable progress towards this goal is shown in Fig. 16, where a Bi atom in Si is moved column-by-column in a controlled fashion.[60] To move the atom, the scanning is stopped and the beam is placed over the target atomic column adjacent to the Bi dopant. The strain field of the large Bi atom makes it energetically favorable to generate a Si vacancy next to the Bi atom, into which the Bi atom then hops. The process is repeated to move the Bi as desired. Clearly, with improved depth resolution, the process could be generalized to three dimensions.

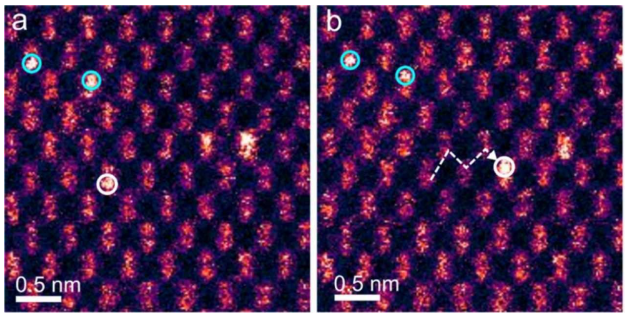


Fig. 16. Electron-beam-directed placement of a Bi atom in Si ⟨110⟩. At 200 kV, the Bi dopant, indicated with a white circle, is moved several unit cells, column-by-column, following the path of the electron beam (marked with white dashed arrows). Blue circles indicate the reference Bi dopants that do not move between frames. Adapted from Ref. [60].

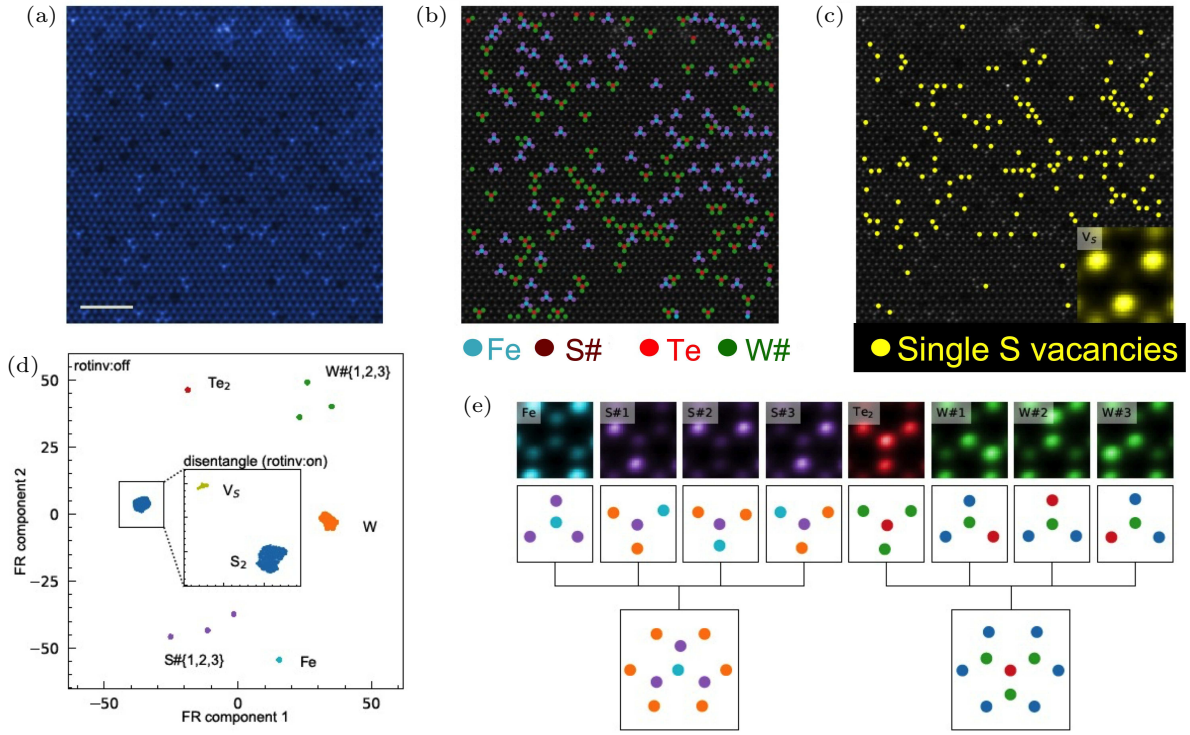


Fig. 17. Identification of dopant sites in a quaternary alloy based on monolayer WS_2. (a) Low-angle ADF-STEM image of monolayer WS_2 doped with Fe and Te. Scale bar, 2 nm. The framework readily identifies (b) Fe-centered (turquoise) and Te-centered (red) motifs, as well as (c) single S vacancies V_S (yellow) within the WS_2 lattice (gray). (d) Force-relaxed (FR) clustering of Zernike features (rotation invariance turned off) shows the W-centered motifs (orange) and S-centered motifs (blue), plus the structural motifs that contain dopants (Fe and Te) or have peripheral S or W atom columns (i.e., S#{1,2,3} and W#{1,2,3}). Among the motifs comprising only W + S, those that are centered on S vacancies can be identified by turning on rotational invariance (inset). (e) For the motifs containing dopants, their spatial context can be summarized as a tree-like hierarchy with other motifs. Adapted from Ref. [61].

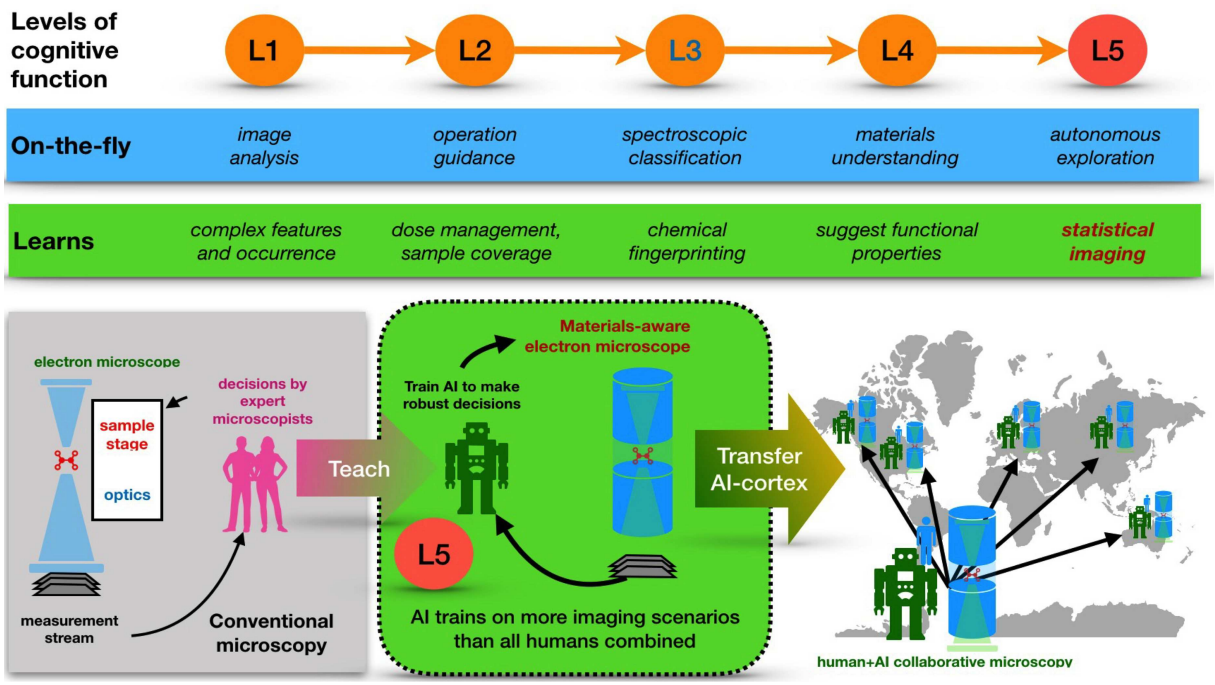


Fig. 18. Schematic showing the stages in the development of a smart, self-driving microscope, with increasing levels of cognitive function, to transition from the expert operators of today to a materials-aware microscope of the future. Such machines could easily be interconnected to increase their experience and interpretative power. Courtesy Duane Loh.

Finally, we can expect an increasing role for machine learning and artificial intelligence in image analysis. An unsupervised scheme is most suitable, since we do not know a priori what kind of defects to expect. Also, it is important that the analysis includes the local atomic configuration, not just identify atom locations. Such a framework has recently been developed based on Zernike polynomial decomposition of local image patches. Zernicke polynomials are very suitable for capturing local symmetry, and very insensitive to image noise. Automatic classification of point defects in monolayer WS_2 doped with Fe and Te is shown in Fig. 17.[61] Once classified, all images of the same classification types can be summed to improve statistics and compared to simulations for identification.

Such schemes could be easily extended to include automatic searching across the sample, a kind of "self-driving" microscope, saving the many hours humans typically spend searching manually for interesting features. Indeed, different samples could be compared, grown under different conditions, and correlated with properties to determine which specific defects determine which function. We can even envisage a world-wide web of microscope data, as shown schematically in Fig 18, all analyzed by artificial intelligence.

6. Summary

Electron microscopy allows deep insights into numerous aspects of physics, including demonstrations of fundamental quantum mechanical principles, the physics of coherent and incoherent imagings, and the physics of materials, whether for understanding the atomic origin of materials properties or to find guidance for the development of new and improved materials. From all these different perspectives, today's microscopes are quite awe-inspiring. Indeed, it seems fair to say there has never been a more exciting time in the history of the microscope. But the promise for the future, with the incorporation of AI into microscopy would appear to offer even more exciting possibilities.

References

[1] Batelaan H and Tonomura A 2009 *Phys. Today* **62** 38
[2] Merli P G, Missiroli G F and Pozzi G 1976 *Am. J. Phys.* **44** 306
[3] Tonomura A, Endo J, Matsuda T, Kawasaki T and Ezawa H 1989 *Am. J. Phys.* **57** 117
[4] Rayleigh L 1896 *Phil. Mag.* **42** 167
[5] Pennycook S J 2012 *Ultramicroscopy* **123** 28
[6] Pennycook S J 2012 *MRS Bulletin* **37** 943
[7] Pennycook S J 2017 *Ultramicroscopy* **180** 22
[8] Cowley J 1969 *Appl. Phys. Lett.* **15** 58
[9] Zeitler E and Thomson M 1970 *Optik* **31** 258
[10] Glauber R and Schomaker V 1953 *Phys. Rev.* **89** 667
[11] Oxley M P, Lupini A R and Pennycook S J 2016 *Rep. Prog. Phys.* **80** 026101
[12] Peng Y, Oxley M P, Lupini A R, Chisholm M F and Pennycook S J 2008 *Microsc. Microanal.* **14** 36
[13] Findlay S D, Shibata N, Sawada H, Okunishi E, Kondo Y, Yamamoto T and Ikuhara Y 2009 *Appl. Phys. Lett.* **95** 191913
[14] Findlay S D, Shibata N, Sawada H, Okunishi E, Kondo Y and Ikuhara Y 2010 *Ultramicroscopy* **110** 903
[15] Knoll M and Ruska E 1932 *Zeit. Physik* **78** 318
[16] von Ardenne M 1938 *Zeit. Physik* **109** 553
[17] Crewe A V 1966 *Science* **154** 729
[18] Crewe A V, Eggenberger D N, Wall J and Welter L M 1968 *Rev. Sci. Instrum.* **39** 576
[19] Pennycook S J 2011 *Scanning Transmission Electron Microscopy* (Pennycook S J & Nellist P D, Ed.) pp. 1–90 (Springer New York)
[20] Cowley J M 1984 *Bull. Mater. Sci.* **6** 477
[21] Pennycook S J and Jesson D E 1990 *Phys. Rev. Lett.* **64** 938

[22] Pennycook S J, Browning N D, McGibbon M M, McGibbon A J, Jesson D E and Chisholm M F 1996 *Phil. Trans. Roy. Soc. A* **354** 2619

[23] Yan Y and Pennycook S J 2000 *Nature* **403** 266

[24] McGibbon A J, Pennycook S J and Angelo J 1995 *Science* **269** 519

[25] Nellist P D and Pennycook S J 1996 *Science* **274** 413

[26] Yan Y, Chisholm M F, Duscher G, Maiti A, Pennycook S J and Pantelides S T 1998 *Phys. Rev. Lett.* **81** 3675

[27] Browning N D, Chisholm M F and Pennycook S J 1993 *Nature* **366** 143

[28] Batson P E, Dellby N and Krivanek O L 2002 *Nature* **418** 617

[29] Nellist P D, Chisholm M F, Dellby N, Krivanek O L, Murfitt M F, Szilagyi Z S, Lupini A R, Borisevich A, Sides W H and Pennycook S J 2004 *Science* **305** 1741

[30] Varela M, Findlay S D, Lupini A R, Christen H M, Borisevich A Y, Dellby N, Krivanek O L, Nellist P D, Oxley M P, Allen L J and Pennycook S J 2004 *Phys. Rev. Lett.* **92** 095502

[31] Krivanek O L, Chisholm M F, Nicolosi V, Pennycook T J, Corbin G J, Dellby N, Murfitt M F, Own C, Szilagyi Z S, Oxley M P, Pantelides S T and Pennycook S J 2010 *Nature* **464** 571

[32] Zhou W, Kapetanakis M D, Prange M P, Pantelides S T, Pennycook S J and Idrobo J C 2012 *Phys. Rev. Lett.* **109** 206803

[33] Ishikawa R, Mishra R, Lupini A R, Findlay S D, Taniguchi T, Pantelides S T and Pennycook S J 2014 *Phys. Rev. Lett.* **113** 155501

[34] Li C, Wu Y, Poplawsky J, Pennycook T J, Paudel N, Yin W, Haigh S J, Oxley M P, Lupini A R, Al-Jassim M, Pennycook S J and Yan Y 2014 *Phys. Rev. Lett.* **112** 156103

[35] Wu H, Zhang Y, Wu J, Wang J and Pennycook S J 2019 *Adv. Funct. Mater.* **29** 1902911

[36] Liu H, Wu H, Ong K P, Yang T, Yang P, Das P K, Chi X, Zhang Y, Diao C, Wong W K A, Chew E P, Chen Y F, Tan C K I, Rusydi A, Breese M B H, Singh D J, Chen L Q, Pennycook S J and Yao K 2020 *Science* **369** 292

[37] Waqar M, Wu H, Ong K P, Liu H, Li C, Yang P, Zang W, Liew W H, Diao C, Xi S, Singh D J, He Q, Yao K, Pennycook S J and Wang J 2022 *Nat. Commun.* **13** 3922

[38] Zhao X, Ning S, Fu W, Pennycook S J and Loh K P 2018 *Adv. Mater.* **30** 1802397

[39] Zhao X, Song P, Wang C, Riis-Jensen A C, Fu W, Deng Y, Wan D, Kang L, Ning S, Dan J, Venkatesan T, Liu Z, Zhou W, Thygesen K S, Luo X, Pennycook S J and Loh K P 2020 *Nature* **581** 171

[40] Tian H, Ma Y, Li Z, Cheng M, Ning S, Han E, Xu M, Zhang P F, Zhao K, Li R, Zou Y, Liao P, Yu S, Li X, Wang J, Liu S, Li Y, Huang X, Yao Z, Ding D, Guo J, Huang Y, Lu J, Han Y, Wang Z, Cheng Z G, Liu J, Xu Z, Liu K, Gao P, Jiang Y, Lin L, Zhao X, Wang L, Bai X, Fu W, Wang J Y, Li M, Lei T, Zhang Y, Hou Y, Pei J, Pennycook S J, Wang E, Chen J, Zhou W and Liu L 2023 *Nature* **615** 56

[41] Zhao X, Dan J, Chen J, Ding Z, Zhou W, Loh K P and Pennycook S J 2018 *Adv. Mater.* **30** 1707281

[42] Shibata N, Findlay S D, Kohno Y, Sawada H, Kondo Y and Ikuhara Y 2012 *Nat. Phys.* **8** 611

[43] Shibata N, Seki T, Sanchez-Santolino G, Findlay S D, Kohno Y, Matsumoto T, Ishikawa R and Ikuhara Y 2017 *Nat. Commun.* **8** 15631

[44] Yang H, Rutte R N, Jones L, Simson M, Sagawa R, Ryll H, Huth M, Pennycook T J, Green M L H, Soltau H, Kondo Y, Davis B G and Nellist P D 2016 *Nat. Commun.* **7** 12532

[45] Pennycook T J, Lupini A R, Yang H, Murfitt M F, Jones L and Nellist P D 2015 *Ultramicroscopy* **151** 160

[46] Yang H, Pennycook T J and Nellist P D 2015 *Ultramicroscopy* **151** 232

[47] Gao C, Hofer C, Jannis D, Béché A, Verbeeck J and Pennycook T J 2022 *Appl. Phys. Lett.* **121** 081906

[48] Jannis D, Hofer C, Gao C, Xie X, Béché A, Pennycook T J and Verbeeck J 2022 *Ultramicroscopy* **233** 113423

[49] Jiang Y, Chen Z, Han Y, Deb P, Gao H, Xie S, Purohit P, Tate M W, Park J, Gruner S M, Elser V and Muller D A 2018 *Nature* **559** 343

[50] Sha H, Cui J and Yu R 2022 *Sci. Adv.* **8** eabn2275

[51] Sha H, Ma Y, Cao G, Cui J, Yang W, Li Q and Yu R 2023 *Nat. Commun.* **14** 162

[52] Ishikawa R, Pennycook S J, Lupini A R, Findlay S D, Shibata N and Ikuhara Y 2016 *Appl. Phys. Lett.* **109** 163102

[53] Chung J Y, Li Z, Goodman S A, So J, Syaranamual G J, Mishra T P, Fitzgerald E A, Bosman M, Lee K, Pennycook S J and Gradečak S 2021 *ACS Photon.* **8** 2853

[54] Li M, Chen P, Zhang Y, Zhang Y, Liu Z, Tang C, Chung J Y, Gu M, Li J, Huang Z, Chow G M, Li C and Pennycook S J 2023 *Small* **19** 2203201

[55] Ishikawa R, Lupini A R, Hinuma Y and Pennycook S J 2015 *Ultramicroscopy* **151** 122

[56] He W, Wang D, Wu H, Xiao Y, Zhang Y, He D, Feng Y, Hao Y J, Dong J F, Chetty R, Hao L, Chen D, Qin J, Yang Q, Li X, Song J M, Zhu Y, Xu W, Niu C, Wang G, Liu C, Ohta M, Pennycook S J, He J, Li J F and Zhao L D 2019 *Science* **365** 1418

[57] Jiang B, Yu Y, Cui J, Liu X, Xie L, Liao J, Zhang Q, Huang Y, Ning S, Jia B, Zhu B, Bai S, Chen L, Pennycook S J and He J 2021 *Science* **371** 830

[58] Idrobo J C, Lupini A R, Feng T, Unocic R R, Walden F S, Gardiner D S, Lovejoy T C, Dellby N, Pantelides S T and Krivanek O L 2018 *Phys. Rev. Lett.* **120** 095901

[59] Yu Y, Xie L, Pennycook S J, Bosman M and He J 2022 *Sci. Adv.* **8** eadd7690

[60] Hudak B M, Song J, Sims H, Troparevsky M C, Humble T S, Pantelides S T, Snijders P C and Lupini A R 2018 *ACS Nano* **12** 5873

[61] Dan J, Zhao X, Ning S, Lu J, Loh K P, He Q, Loh N D and Pennycook S J 2022 *Sci. Adv.* **8** eabk1005